

**Long-range order in arrays of composite and monolithic magnetotoroidal moments**Jannis Lehmann <sup>1,2,\*</sup>, Naëmi Leo <sup>3,4,5,6</sup>, Laura J. Heyderman <sup>3,4</sup> and Manfred Fiebig <sup>1,†</sup><sup>1</sup>Laboratory for Multifunctional Ferroic Materials, Department of Materials, ETH Zurich, 8093 Zurich, Switzerland<sup>2</sup>RIKEN Center For Emergent Matter Science (CEMS), Wako, Saitama 351-0198, Japan<sup>3</sup>Laboratory for Mesoscopic Systems, Department of Materials, ETH Zurich, 8093 Zurich, Switzerland<sup>4</sup>Laboratory for Multiscale Materials Experiments, Paul Scherrer Institute, 5232 Villigen PSI, Switzerland<sup>5</sup>Nanomagnetism Group, CIC nanoGUNE BRTA, 20018 Donostia, San Sebastián, Spain<sup>6</sup>Instituto de Nanociencia y Materiales de Aragón (INMA), CSIC, Universidad de Zaragoza, 50009 Zaragoza, Spain

(Received 8 April 2022; revised 12 July 2023; accepted 24 July 2023; published 5 September 2023)

Magnetotoroidal order, also called ferrotoroidicity, is the most recently established type of ferroic state. It is based on a spontaneous and uniform alignment of unit-cell-sized magnetic whirls, called magnetotoroidal moments, associated with a macroscopic toroidization. Because of its intrinsic linear magnetoelectric coupling, this new ferroic state could be useful in the development of spintronic devices. We exploit two-dimensional periodic arrays of magnetostatically coupled nanomagnets as model systems for the investigation of long-range magnetotoroidal order. We present two pathways promoting this order, namely, (i) structures comprising a ring of uniformly magnetized sub-micrometer-sized bar magnets and (ii) structures in which each magnetic building block itself hosts a magnetic vortex. For both cases, calculations of the magnetic-dipole interaction and micromagnetic simulations reveal the conditions for the formation of spontaneous magnetotoroidal order. We confirm this order and the formation of magnetotoroidal domains in our arrays with magnetic force microscopy. We identify the presence of two types of domain-wall states emerging from the competition of two intrinsic microscopic couplings. Our work not only identifies the microscopic conditions promoting spontaneous magnetotoroidal order but also highlights the possibility to tailor mesoscale magnetic arrays toward elusive types of ferroic order.

DOI: [10.1103/PhysRevB.108.104405](https://doi.org/10.1103/PhysRevB.108.104405)**I. INTRODUCTION**

The search for self-organized ordered or strongly correlated states of matter is a fascinating subject of physics and materials science. Ferroic materials, which are related to a spontaneous and reorientable magnetic, electric, or structural order [1–3], are of particular interest as they provide the basis for a plethora of technological applications. Ferroic materials are defined by the existence of a spontaneous point-group-symmetry-breaking phase transition with the formation of domains as regions described by different, yet uniform orientations of the so-called order parameter as a macroscopic observable classifying the phase transition. This order parameter, which may be the magnetization in the case of ferromagnetism, has to be orientable by a conjugate field, which, for the magnetization, is a magnetic field. Importantly, beyond this purely macroscopic definition, ferroic materials require microscopic interactions that support and stabilize the associated spin, charge, or distortive order. The identification and understanding of new types of ferroic states complementing the established ones (ferromagnetism, ferroelectricity, and ferroelasticity [2]) is a task of great current interest [4,5]. In this respect, ferrotoroidicity has recently been proposed as a ferroic state defined by the spontaneous uniform long-range alignment of magnetic whirls, the so-called magnetotoroidal

moments [6–11]. As shown in Fig. 1, these toroidal moments can be composed from an arrangement of elementary magnetic moments within the unit cell, or they may be exhibited monolithically by the elements themselves, for instance, in the form of orbital currents [4,12,13].

The uniform alignment of the magnetotoroidal moments  $\mathbf{t}$  leads to a macroscopic toroidization  $\mathbf{T}$  representing the order parameter; see Fig. 2. The configuration of magnetic moments associated with the ferrotoroidic state breaks the space-inversion and time-reversal symmetries, with fundamental consequences for related electric and magnetic responses and couplings. Specifically, magnetotoroidal materials allow for an electric-field-induced magnetization and a magnetic-field-induced polarization via the linear magnetoelectric effect [9,14–16]. Ferrotoroidic materials may thus be exploited for nanoelectronic memories or sensors that are based on intertwined magnetic and electric properties. Furthermore, the linear magnetoelectric effect in the optical regime manifests as directional anisotropy and thus opens a pathway for photonic devices such as optical diodes [17–21].

The scarcity of studies on imaging and manipulation of ferrotoroidic domains [22,23] is largely due to the magnetically compensated nature of the ferrotoroidic state, which hampers experimental access to and thus a deeper understanding of the concept of magnetotoroidal order. In addition, it is difficult to disentangle the fragile competition of exchange interactions that is assumed to promote the toroidal order on the microscopic scale [9,11,24]. To overcome these obstacles, we take advantage of the definition of ferroic order

\*jannis.lehmann@posteo.de

†manfred.fiebig@mat.ethz.ch

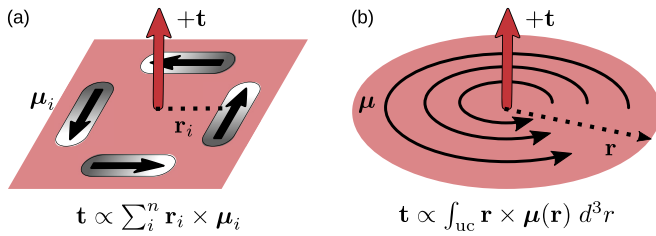


FIG. 1. Two-dimensional microscopic representations of magnetotoroidal moments. (a) Composite magnetotoroidal moment  $\mathbf{t}$  originating either from discrete quantum-mechanical spins or from a classical magnetic-moment density  $\mu_i$  (black arrows and contrast gradients) displaced by distance vectors  $\mathbf{r}_i$  from the origin. (b) Monolithic magnetotoroidal moment originating either from localized orbital currents of atoms or ions, or from a continuous vortexlike magnetization configuration within a single magnetically ordered entity.

as a macroscopic phenomenon, irrespective of its explicit microscopic origin. As shown in Refs. [25,26], a transfer from the atomic to the sub-micrometer length scale, or mesoscale, provides a means to implement and probe ferrotoroidicity to a degree that conventional “atomic” materials cannot offer. For these studies, the quantum-mechanical magnetic moments of a hypothetical magnetotoroidal crystal are replaced by classical macrospins in the form of magnetic single-domain sub-micrometer-sized permalloy bars, that can be lithographically patterned and arranged at will, thus allowing versatile tailoring of the symmetry and microscopic interactions of the resulting array.

In the work presented in this article, we build on studies of conjugate-field poling [25] and manipulation of short- and long-range order [26] in artificial magnetotoroidal crystals. These previous studies were performed on a single and very specific type of magnetotoroidal array. We now present a variety of mesoscale magnetic systems, either composed of single-domain bars or of equilateral triangles, as two fundamentally different types of building blocks for magnetotoroidal arrays. While in the former case a ringlike arrangement of the magnetic-dipole-like building blocks [27] exhibits a composite magnetotoroidal moment, the latter hosts a monolithic magnetotoroidal moment in each individual building block [28,29]. Using magnetic-dipole calculations and micromagnetic simulations, we quantify and tailor two variants of microscopic interactions that are required to promote ferrotoroidic ordering in these two types of systems—an intra- and an intertoroidal coupling. Using magnetic force microscopy (MFM) we confirm the existence of as-grown magnetotoroidal domains, and we resolve the domain-wall states in our nanomagnetic structures.

The article is organized as follows: In Sec. II we explain how we fabricate and probe our magnetotoroidal arrays, as well as how we perform micromagnetic simulations. The composite and monolithic types of magnetotoroidal moments that provide the basis for the spontaneous formation of magnetotoroidal order are introduced in Sec. III. We quantify the microscopic interactions between the building blocks and demonstrate the implementation of suitable couplings in arrays of composite and monolithic magnetotoroidal moments in Secs. IV A and IV B, respectively. In Sec. IV C we intro-

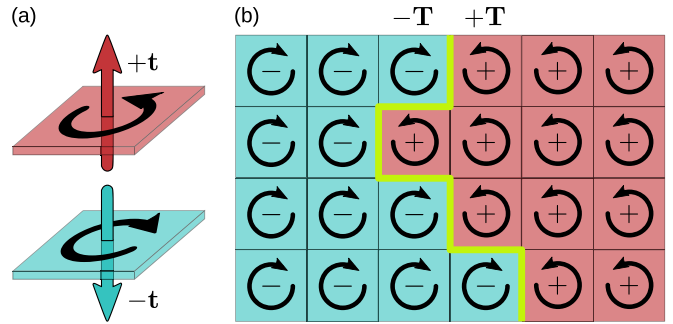


FIG. 2. Magnetotoroidal domain structure. (a) Representation of the two magnetotoroidal-moment orientations (cyan:  $-\mathbf{t}$ , red:  $+\mathbf{t}$ ) with magnetic moments in a clockwise or counterclockwise head-to-tail orientation (black circular arrow). (b) Magnetotoroidal domain structure in which a domain wall (green line) separates states with a toroidization of  $-T$  (cyan) and  $+T$  (red).

duce our processing of MFM data to identify the associated toroidal order. In Sec. V, we present and discuss the experimental data on magnetotoroidal domains and domain-wall configurations. We summarize our findings and put them into the larger context of magnetically compensated ferroic order in Sec. VI.

## II. METHODS

### A. Sample fabrication

Arrays of sub-micrometer-sized building blocks made from ferromagnetic permalloy ( $\text{Ni}_{81}\text{Fe}_{19}$ ) were fabricated using electron-beam lithography and electron-beam evaporation at room temperature. For this, a polymethyl methacrylate layer (2% PMMA 950k) was spin-coated onto a 500- $\mu\text{m}$ -thick (100)-oriented silicon substrate. An electron-beam writer (Vistec EBPG 500Plus) operating with an acceleration voltage of 100 kV at a dose of about 600  $\mu\text{C}/\text{cm}^2$  was used to write the pattern into the PMMA resist. After development, permalloy thin films with thicknesses between 12 and 20 nm were deposited via electron-beam evaporation at a growth rate of 0.3  $\text{nm min}^{-1}$  and at a base pressure of  $10^{-6}$  mbar. The polycrystalline nature of the permalloy film, with its negligible magnetocrystalline anisotropy, ensures a distribution of the local magnetization within each building block that is determined primarily by its shape. A thin capping layer of a few nanometers of gold or aluminum was deposited on top of the permalloy to prevent deterioration due to permalloy oxidation. Afterwards, the remaining resist and unwanted material were removed via ultrasound-assisted lift-off in Technistrip P1316. The resulting arrays have lateral sizes of about  $50 \times 50 \mu\text{m}^2$ .

### B. Micromagnetic imaging

To probe the magnetotoroidal configuration in our arrays, we performed MFM (using an NT-MDT NTegra-Prima system) by applying the two-pass measuring principle in tapping mode with an oscillating tip. We measure the topography profile in the first scan in close proximity to the surface. In a second scan, this topography profile is retraced at a lift height of typically 40 to 50 nm, to sense the out-of-plane magnetic stray-field gradient. We used tips with a low magnetic moment

(Nanosensors PPP-LM-MFMR) to avoid tip-induced changes of the magnetic order.

### C. Micromagnetic simulations

The magnetic configuration and stray fields of the triangle-shaped building blocks, see Sec. IV, were simulated using the program Mumax<sup>3</sup> [30]. The geometric parameters of a single building block were discretized into a grid with cells of  $2 \times 2 \times 4 \text{ nm}^3$  (length  $\times$  width  $\times$  height). To simulate the magnetic configuration of the triangle, we use bulk values for the saturation magnetization,  $M_{\text{sat}} = 860 \text{ kA m}^{-1}$  and the exchange stiffness,  $A_{\text{ex}} = 13 \text{ pJ m}^{-1}$ , and a vanishing anisotropy ( $K = 0$ ) [31]. The magnetic stray field is calculated for a single triangle-shaped building block surrounded by vacuum.

## III. MODELING TOROIDAL ORDER ON THE MESOSCALE

For implementing magnetotoroidal order in two-dimensional arrays of nanomagnets, two design criteria have to be considered. First, the artificial unit cells of the arrays have to exhibit a magnetotoroidal moment as the basis of the macroscopic order. This toroidal moment can either be formed as a composite of  $n$  magnetic moments  $\mu_i$  located at positions  $\mathbf{r}_i$  in the unit cell, see Fig. 1(a) [ $\mathbf{t} \propto \sum_{i=1}^n \mathbf{r}_i \times \mu_i$ ], or it originates from a continuous magnetic curl [ $\mathbf{t} \propto \int_{\text{uc}} \mathbf{r} \times \boldsymbol{\mu}(\mathbf{r}) d^3r$  with  $\boldsymbol{\mu}(\mathbf{r})$  as the magnetic-moment density and “uc” denominating the unit cell] forming a monolithic toroidal moment; see Fig. 1(b). Second, since toroidal order refers to the spontaneous uniform alignment of these toroidal moments, a nonzero net toroidization  $\mathbf{T} = N^{-1} \sum_{j=1}^N \mathbf{t}_j$ , with  $N$  as the number of unit cells contributing to the uniform alignment, has to emerge as the corresponding order parameter. This leads to the formation of toroidal domains, as schematically shown in in Fig. 2(b). Note that the replacement of spins of the ions in conventional crystals with macrospins of the magnetic nanobars in our mesoscale arrays goes hand-in-hand with the substitution of the quantum-mechanical exchange interaction with the classical magnetic-dipole interaction between the building blocks [32–34].

In this work, we investigate arrays of nanomagnets based on two complementary types of building blocks promoting magnetotoroidal order. These building blocks are made of ferromagnetic polycrystalline permalloy, with a negligible magnetocrystalline anisotropy, where the shape of the nanoscale element determines its internal magnetic structure [35]. The first set of arrays consists of stadium-shaped bars, each with a length of  $l = 450 \text{ nm}$ , a width of  $w = 150 \text{ nm}$ , and a circular end with radius of curvature of  $r = w/2 = 75 \text{ nm}$ ; see Fig. 3(a). The ferromagnetic bars are single domain with an in-plane magnetization pointing along their long axis; see Fig. 3(c). Hence, these Ising-like macrospins are a classical representation of quantum-mechanical spins [36]. Such macrospins have been successfully used to address fundamental questions about magnetic correlations, frustration, thermal relaxation, phase transitions, and many other phenomena [37].

The second set of arrays consists of equilateral triangles with  $l = 400 \text{ nm}$  edge length and  $r = 50 \text{ nm}$  corner radius of curvature; see Fig. 3(b). The appropriate choice of trian-

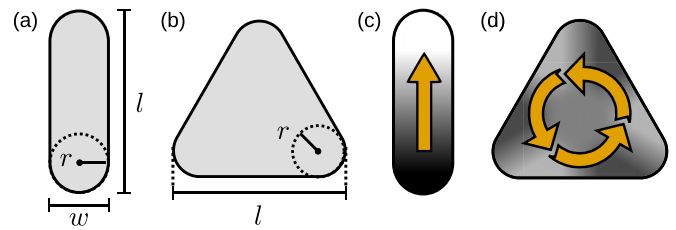


FIG. 3. Ferromagnetic constituents of composed and monolithic toroidal moments. Our arrays are composed of (a) nanobars and (b) equilateral planar triangles arranged in different tilings; see Figs. 4 and 5. Adjustable parameters are the length  $l$ , the width  $w$ , the radius of curvature  $r$ , and the height  $h$ . (c) The nanobars exhibit a magnetic single-domain state with magnetization pointing in one of two directions parallel to the long axis of the bar (orange arrow and contrast gradient) corresponding to an Ising-like degree of freedom. (d) The equilateral triangles exhibit a clockwise or counterclockwise magnetic vortex associated with a down or up toroidal moment.

gle size, corner radius and thickness allows us to promote the formation of a magnetic vortex [38] as indicated in Fig. 3(d). The triangular shape breaks the in-plane rotational symmetry and, in contrast to circular-shaped building blocks, supports nonzero magnetic stray fields [28,29,39]. The stray field emanating from each magnetic triangle facilitates their magnetostatic coupling, which is required for the emergence of spontaneous long-range order. In addition, the stray fields allow for the detection of the magnetic configuration with MFM.

Unlike in conventional ionic crystals, a phase transition promoting a macroscopic toroidization via a structural distortion [8] is currently not feasible; the particular magnetic-moment configuration on our lattices as such breaks space-inversion and time-reversal symmetries. Furthermore, all the arrays presented here exhibit zero net magnetization, so that a decomposition into an uncompensated (magnetized) and a compensated (toroidal) part of the spin arrangements as described in Ref. [8] is not necessary.

Considering one of the key aspects of ferroic materials—the reversibility of the order parameter in a conjugate field—noncentrosymmetric arrays of triangle-shaped magnetotoroidal elements, see Fig. 5(c), offer interesting possibilities. Such arrays facilitate the controlled reversal of the toroidization simply by the application of a homogeneous magnetic field due to the asymmetric nucleation energy of the vortex core [39,40]. This feature is a striking advantage in terms of applications based on the array’s net toroidization.

## IV. ENGINEERING OF MICROSCOPIC INTERACTIONS

To identify arrangements of magnetic building blocks that promote a magnetotoroidal ordering, we limit our considerations to the magnetostatic interaction between direct neighbors. This approximation is justified by the rapid  $r^{-3}$  decay of the dipolelike magnetic stray field with distance,  $r$ . We have provided a verification in Appendix A 1 showing that more sophisticated models result in corrections to the interaction energies of less than 10% with no qualitative changes in the resulting magnetic order.

We distinguish between two types of couplings: First, the distribution of magnetic stray fields within each basic unit has

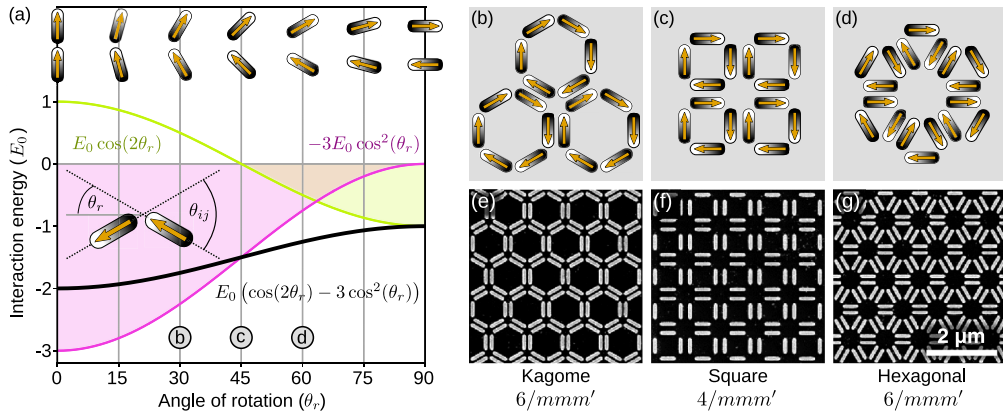


FIG. 4. Magnetic coupling in arrays of composite toroidal moments. (a) Angle-dependent interaction energies, see Eq. (2), for pairs of magnetic moments as schematically shown in the upper part of the panel. The purple and green curves represent the two types of couplings given by Eq. (2) and quantify the contribution of the coupling terms to the total magnetic-dipole interaction energy (black curve). The assumption of a constant center-to-center distance between the magnets and the simplification of representing the nanobars as pairwise interacting point dipoles captures the behavior of our systems qualitatively (see Appendix A 1). [(b)–(d)] Schematics of a kagome lattice at  $\theta_r = 30^\circ$  (b), a square lattice at  $\theta_r = 45^\circ$  (c), and a hexagonal lattice at  $\theta_r = 60^\circ$  (d) in a  $-\mathbf{t}$  configuration. [(e)–(g)] Corresponding scanning electron microscopy images showing sections of the three arrays. Arrays (e) and (g) are composed of 12-nm-thick permalloy bars of size  $l = 450$  nm and  $w = 150$  nm whereas the permalloy thickness of building blocks in array (f) is 20 nm. The scale bar is the same for all of the arrays [(e)–(g)].

to favor a compensated, whirl-like configuration of magnetic moments, a condition we denote as “intratoroidal coupling”. Second, the magnetic stray fields exhibited by these magnetotoroidal building blocks promote a parallel orientation of adjacent toroidal moments, a condition we denote as “inter-toroidal coupling”. For the arrays of composite and monolithic magnetotoroidal moments, these two types of coupling have fundamentally different origins with consequences for the emergent domain structure in the arrays, as we will explain in more detail.

#### A. Interactions in arrays of composite magnetotoroidal moments

For the arrays of composite magnetotoroidal moments, both the intra- and intertoroidal couplings originate from the magnetic-dipole-like stray fields generated by the magnetic single-domain bars. The coupling energy  $E_D$  of two interacting bars can be approximated by the magnetic dipole-dipole interaction between two point dipoles according to

$$E_D = \frac{\mu_0}{4\pi} \left( \frac{\mathbf{m}_i \cdot \mathbf{m}_j}{|\mathbf{r}_{ij}|^3} - \frac{3(\mathbf{m}_i \cdot \mathbf{r}_{ij})(\mathbf{m}_j \cdot \mathbf{r}_{ij})}{|\mathbf{r}_{ij}|^5} \right), \quad (1)$$

where  $\mu_0$  is the vacuum permeability,  $\mathbf{m}_{i,j}$  are vectors of the  $i$ th and  $j$ th magnetic moment, and  $\mathbf{r}_{ij}$  is the vector connecting the two. Equation (1) can be rewritten by considering just the angle  $\theta_{ij} = \arccos[(\mathbf{m}_i \cdot \mathbf{m}_j)/(|\mathbf{m}_i| |\mathbf{m}_j|)]$  between the two neighboring magnetic moments  $\mathbf{m}_{i,j}$ . We here limit ourselves to arrays in which neighboring magnets are placed as depicted in the upper panel of Fig. 4(a) and with a fixed distance  $|\mathbf{r}_{ij}|$  between their centers. We can now express Eq. (1) as a function of the angle  $\theta_r = \arccos[(\mathbf{m}_i \cdot \mathbf{r}_{ij})/(|\mathbf{m}_i| |\mathbf{r}_{ij}|)] = \theta_{ij}/2$  between a magnetic moment and the distance vector  $\mathbf{r}_{ij}$  to its nearest neighbor, as

$$E_D = E_0 [\cos(2\theta_r) - 3\cos^2(\theta_r)], \quad (2)$$

with  $E_0 = (\mu_0 |\mathbf{m}_{i,j}|^2)/(4\pi |\mathbf{r}_{ij}|^3)$ .

To construct composite magnetotoroidal moments from macrospins, we place them in a circular arrangement forming the unit cell of the array. Here we choose arrangements made of six ( $2\theta_r = 60^\circ$ ), four ( $2\theta_r = 90^\circ$ ), or three ( $2\theta_r = 120^\circ$ ) magnets forming kagome, square, and hexagonal lattices, respectively; see Figs. 4(b)–4(d). As shown in Fig. 4(a), the intratoroidal coupling that stabilizes a whirl-like magnetic configuration within the unit cell is mainly promoted by the second term of Eq. (2) (purple line). In the same manner, the intertoroidal coupling that connects the magnetic whirls across the unit cells is represented by the first term in Eq. (2) (green line). In all our arrangements, the intertoroidal coupling manifests itself as the antiparallel alignment of magnetic moments from neighboring unit cells at  $2\theta_r = 180^\circ$ .

#### B. Interactions in arrays of monolithic magnetotoroidal moments

In contrast to the magnetic-dipole interaction determining the order in arrays of composite magnetotoroidal moments, the microscopic interactions promoting long-range order in arrays of monolithic magnetotoroidal moments are of a fundamentally different nature. In particular, the intra- and intertoroidal couplings have separate sources. The intratoroidal coupling results from competing contributions to the free energy within the individual ferromagnetic building block, which are primarily due to the magnetostatic interaction favoring flux-closed configurations of magnetic moments with minimized stray fields and the magnetic exchange interaction striving for a parallel and uniform spin alignment with a maximized magnetization. While the design parameters of the permalloy nanobars shown in Fig. 3(a) can be tailored to obtain a uniformly magnetized macrospinlike configuration, see Fig. 3(c), the permalloy triangles in Fig. 3(b) can be engineered to stabilize a magnetic vortex configuration as shown in Fig. 3(d).

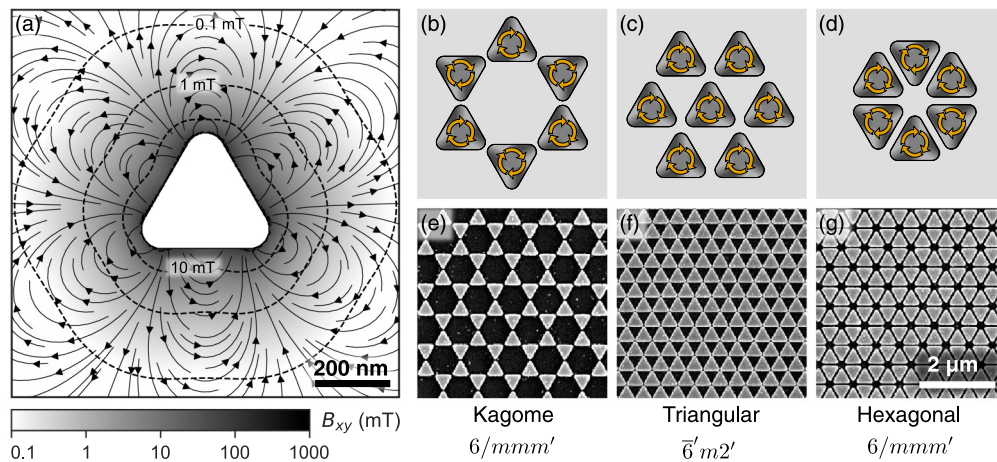


FIG. 5. Magnetic coupling in arrays of monolithic toroidal moments. (a) Micromagnetic simulation of the magnetic field surrounding a 20-nm-thick permalloy triangle of dimensions  $l = 400$  nm and  $r = 50$  nm in its magnetic ground state. The streamlines and contrast indicate the in-plane magnetic-field strength  $B_{x,y}$  in the plane of the triangle. [(b)–(d)] Schematics of triangular magnets on a kagome lattice (b), a triangular lattice (c), and a hexagonal lattice (d) in a  $-\mathbf{t}$  configuration with the specified magnetic point-group symmetry. [(e)–(g)] Corresponding scanning electron microscopy images showing sections of the three arrays. Arrays (e) and (g) are composed of 12-nm-thick permalloy triangles, whereas array (f) is made from 20-nm-thick permalloy triangles. The scale bar is the same for all of the arrays [(e)–(g)].

Instead of a simple dipolelike magnetic field surrounding the uniformly magnetized nanobars, the planar magnetic triangles exhibit a more complicated and inherently weaker hexapolelike magnetic field as shown in Fig. 5(a) as the basis for the intertoroidal coupling. The position of the six magnetic poles of alternating sign surrounding each magnetic triangle determine which arrangements of triangles can promote an intertoroidal coupling. We designed a variety of corner- and edge-coupled networks of magnetic triangles, forming kagome, triangular, and hexagonal lattices, respectively; see Figs. 5(b)–5(d). The proximity of oppositely charged magnetic poles in our structures introduces a coupling that favors locally a parallel alignment of neighboring toroidal moments and, hence, a global toroidization.

### C. Image analysis

We describe here the basic image processing protocols that we applied to proceed from the MFM raw images to the final color-coded magnetotoroidal domain structures. For the composite as well as the monolithic magnetotoroidal arrays, it is key to first identify the magnetization configuration of every single magnetic building block. We can extract the local magnetization directions from the contrast given by the phase response measured in the second pass of the MFM scan [41]; see Sec. II B and Fig. 6(a). The magnetic stray fields that stem from south (north) poles are encoded as white (black) features in the image.

While the assignment of the homogeneous magnetization direction in the bar-shaped dipolar nanomagnets is straightforward, the assignment of the vorticity in the magnetic triangles requires a more careful analysis.

In Fig. 6(b), we show simulated out-of-plane magnetic stray fields from an equilateral permalloy triangle in the two magnetic ground states of opposite magnetic vorticity. The simulation reveals the emergence of six magnetic poles of alternating sign around each triangle that form a propellerlike pattern. This pattern breaks the vertical mirror symmetry of

each triangle as it is rotated by about  $\pm 30^\circ$ , depending on the vorticity. The simulations, as well as the associated literature on planar soft magnetic triangles, e.g. Ref. [42], allow us to interpret our MFM data. Figure 6(c) represents the  $z$ -derivative of the magnetic stray field above the sample surface. By identifying the magnetotoroidal state of each triangle manually, we can colorize an entire MFM scan, see Fig. 6(d), according to the two toroidization directions as defined in Fig. 2(a).

## V. EXAMINATION OF TOROIDAL DOMAIN CONFIGURATIONS

### A. Long-range order in arrays of composite magnetotoroidal elements

Figure 7 shows the magnetotoroidal-domain configurations measured by MFM on the three macrospin-based arrays shown in Figs. 4(e)–4(g). The MFM scans performed on as-grown arrays reveal the local toroidization as well as the structure of the walls separating areas with toroidization  $-\mathbf{T}$  (cyan) and  $+\mathbf{T}$  (red). For all arrays, we find spontaneous magnetotoroidal order with domains that extend laterally over a few to several tens of unit cells. The formation of finite-sized domains can be understood as a freezing-out of a nonequilibrium configuration during the growth of the arrays. With the increasing permalloy film thickness during growth, the energy barrier for switching as well as the coupling strength between neighboring elements increases such that thermal fluctuations are more and more suppressed. As a consequence, the ongoing deposition emulates the continuous decrease of the array's temperature. The magnetization configuration is eventually quenched from a superparamagnetic state through the symmetry-breaking phase transition into a nonequilibrium multidomain configuration when reaching a thickness of typically a few nanometers [43]. Beyond this critical point, the thickness of the structures has no further influence on the magnetic state. Nevertheless, its further increase enhances the dipolar coupling and improves the signal-to-noise

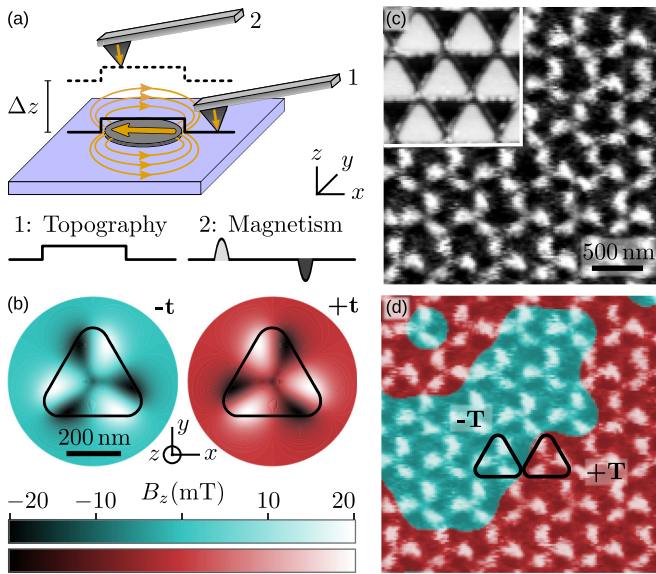


FIG. 6. Image post-processing for visualizing the magnetotoroidal order. (a) Schematic of the two-pass measurement principle in an MFM. We measure the topography in the first line scan (1) in close proximity to the surface using the tapping mode; see the solid line in the schematic. In a second line scan (2), this topography is retraced at a lift height of typically 40 to 50 nm for recording the  $z$ -derivative of the magnetic stray field; see the dashed line in the schematic. A representation of the measured responses for the two line scans are indicated below the schematic. (b) Micromagnetic simulation (see Sect. II for details) of the magnetic field generated by a 20-nm-thick permalloy triangle of dimensions  $l = 400$  nm and  $r = 50$  nm in its two magnetic ground states with  $\pm t$ . The color scale denotes the strength of the  $z$  component of the magnetic stray field 40 nm above the triangle. Note the different arrangement of magnetic poles for the  $-t$  compared with the  $+t$  configuration. (c) MFM scan of an array of equilateral triangles revealing the  $z$ -derivative of the magnetic field 50 nm above the sample surface. The inset shows the topography scan for the area that it replaces. (d) Color-coded MFM image from (c) highlighting the identified orientation of the magnetotoroidal moments. The black outlines indicate two triangles of opposite magnetotoroidal moment; see panel (b). The scale bar is the same for panels (c) and (d).

ratio for the MFM measurements. The average size of the domains as well as the microstructure and density of the domain walls are governed by the domain-wall energy and the number of energetically degenerate domain-wall states. Note that the three arrays were grown at different times so that a qualitative comparison of parameters such as the observed domain size would be impeded by systematic variations and is therefore of limited significance.

### B. Long-range order in arrays of monolithic magnetotoroidal elements

The MFM scans performed on the three triangle-based arrays, see Figs. 5(e)–5(g) are shown in Fig. 8. The measurements reveal spontaneous magnetotoroidal order and domains that extend across a few unit cells. For the kagome and the triangular arrays shown in Figs. 8(a) and 8(b), we found that all permalloy triangles form a magnetic vortex state as shown schematically in Fig. 3(d). Apparently, the intratoroidal cou-

pling dominates in the arrays of monolithic toroidal moments, stabilizing the vortex state in the magnetic triangles against the formation of energetically unfavorable uniformly magnetized configurations without a magnetotoroidal moment. This behavior is a result of the fundamentally different sources of the two types of interactions underlying the long-range order. The intratoroidal coupling that promotes the magnetic vortex as the ground state in each triangle originates from the interplay between the magnetic exchange and magnetostatic interactions. The intertoroidal coupling, in contrast, is a result of the weaker magnetic-multipolar stray fields emanating from each magnetic triangle; see Fig. 5(a). These stray fields affect the internal energy of adjacent triangles, enhancing or lowering the stability of their internal vortex state. Since the magnetic-exchange interaction is inherently stronger than multipolar magnetostatic interactions, the intratoroidal coupling is naturally dominant.

The dense packing of triangles in the hexagonal array shown in Fig. 8(c) reduces the out-of-plane magnetic stray fields and lowers the MFM contrast such that an unambiguous assignment of the toroidal domain structure works in selected areas only, as e.g. shown in the highlighted area in Fig. 8(c). In contrast, at the domain walls, adjacent triangles exhibiting an opposite toroidal moment yield enhanced out-of-plane magnetic stray fields that are well detectable by MFM.

### C. Factors determining the size of magnetotoroidal domains

Domain structures in ferroics are determined by the interplay of intrinsic and extrinsic contributions to the free energy. In the following, we discuss the impact of intrinsic factors (those that are directly associated with the lattice symmetry and geometry) and extrinsic factors (those that depend on the experimental conditions for realizing the arrays) that determine the domain sizes in our arrays.

#### 1. Intrinsic factors

(1) *Angle between neighboring magnetic elements.* As shown in Figs. 4 and 5, the lattice symmetry determines the angle between adjacent magnetic moments, which—due to the anisotropic nature of the magnetic-dipole interaction—has a direct effect on the microscopic coupling strength.

(2) *Number of neighboring magnetic moments per vertex* for arrays of composite magnetotoroidal moments. The symmetry of the structure determines the number of nanomagnets that meet at the vertices of the lattice between the unit cells; see Figs. 4(b)–4(d) and 9. Accordingly, the number of possible configurations of local ensembles of magnetic moments differs between our arrays. Because of the Boltzmann entropy, the probability for domain-wall formation increases statistically with the number of magnetic moments per vertex, in line with the rising number of degenerate domain-wall states; see, e.g., Refs. [43] and [44]. As a consequence, a trend is expected in our arrays, with smaller domains for fewer magnetic moments per ringlike magnetotoroidal moment (and hence more magnetic moments per lattice vertex).

(3) *Size of a unit cell.* Domain sizes in conventional crystals are typically on a different length scale (e.g.,  $10^{-6}$  m to  $10^{-3}$  m) than the dimensions of the unit cell ( $10^{-10}$  m). This is not true for arrays of nanomagnets in which the two length scales approach each other. Therefore, it becomes important

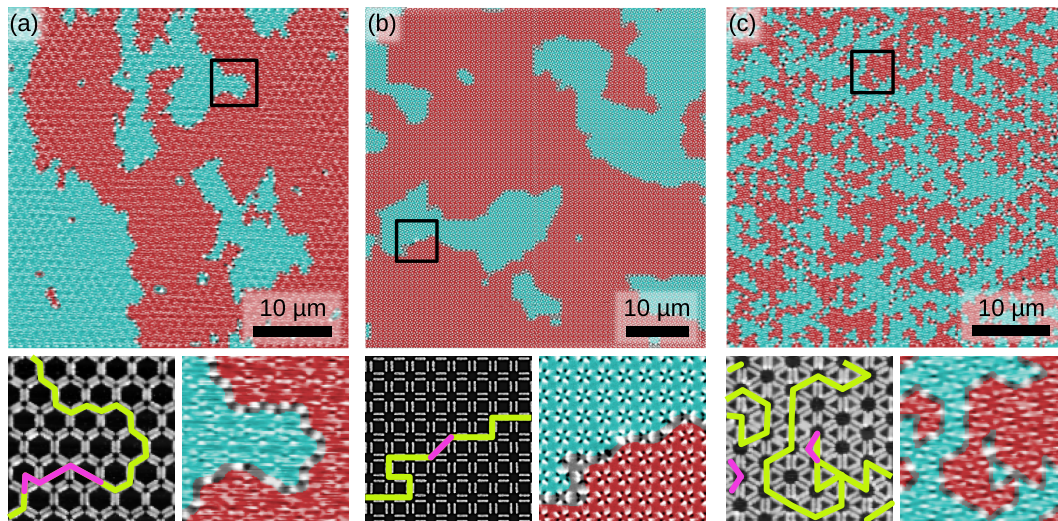


FIG. 7. Long-range order in arrays of composite magnetotoroidal moments. MFM scans with color-coded domain states (cyan:  $-T$ , red:  $+T$ ) of the three arrays with composite magnetotoroidal moments as introduced in Fig. 4. Lower panels: Topography (left) and corresponding magnetotoroidal order (right) of magnified areas around a domain wall. Two types of domain-wall configurations are indicated that run either in between (intertoroidal walls, green lines) or across (intratoroidal walls, purple lines) the magnetotoroidal unit cells. An uncolored version of this figure is given in Fig. 11 in Appendix A 2.

to consider the different unit-cell sizes of various arrays as base units for parametrizing the domain size. Depending on the actual choice of the base unit ( $[\mu\text{m}]$  or  $[\text{u.c.}]$ ), the domain sizes may scale qualitatively differently across our arrays.

## 2. Extrinsic factors

(1) *Distance-dependent coupling strength.* The ratio of the inter- and intratoroidal coupling strength has a pronounced impact on the resulting size and morphology of toroidal domains; see also Ref. [26]. For the experimental systems, the ratio is primarily determined by the distances between neigh-

boring nanomagnets within the array and is, thus, virtually independent of the lattice symmetry and geometry. The weakest of the two couplings determines the effective ordering temperature and, accompanied by this, the length scale for the observed order.

(2) *Thin-film growth rate.* The deposition rate of the ferromagnetic material determines the speed at which the transition from the superparamagnetic regime to the short- and finally long-range-ordered phase occurs. For lower deposition rates, a system has more time to approach the equilibrium state with potentially larger domains.

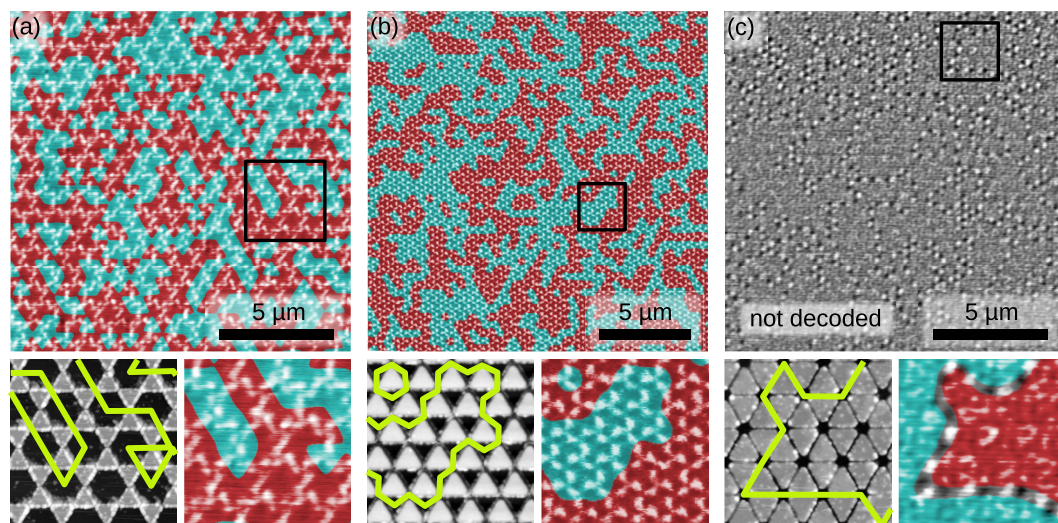


FIG. 8. Long-range order in arrays of monolithic magnetotoroidal moments. MFM scans with color-coded domain states (cyan:  $-T$ , red:  $+T$ ) of the three arrays with monolithic magnetotoroidal moments as introduced in Fig. 4. Lower panels: Topography (left) and corresponding magnetotoroidal order (right) of magnified areas around a domain wall. Due to the monolithic nature of the building blocks, only intertoroidal walls emerge (green lines). An uncolored version of this figure is given in Fig. 12 in Appendix A 2.

(3) *Choice of invariant set of model parameters.* To compare the domain sizes of different arrays of nanomagnets, it is key to select a suitable reference length that remains constant throughout a series of arrays. This may be the nanomagnet center-to-center distance or the edge-to-edge distance (or gap) between neighboring magnetic elements. The trend in the expected domain size for different arrays depends qualitatively on the chosen reference length (in our case a constant gap) that parameterizes the magnetic interactions.

(4) *Boundary effects.* When the domain size approaches the size of the array [see, for example, Fig. 7(b)], the extracted area of the domain will be underestimated due to truncation effects.

#### D. Domain walls and their substructure in magnetotoroidal arrays

Domain walls can be regarded as correlated excitations in ordered systems that originate from the reorientation of the order parameter when moving from one domain to another. The study of domain walls is of fundamental interest as their presence and manipulability determines technological key parameters of ferroic materials, such as their “hardness” in terms of resisting external stimuli, as well as transport properties. Here, the transfer from atomic to mesoscopic magnetotoroidal systems enables unparalleled insights into the nature of the domain walls.

The walls in our magnetotoroidal arrays are highlighted in the lower panels of Figs. 7 and 8. We observe two types of walls, which either run in between or across the magnetotoroidal elements, as indicated in the lower panel of Fig. 7, with green (intertoroidal walls) and purple (intratoroidal walls) lines, respectively. The preferred type of domain-wall state is the one that requires the least amount of energy for its formation, which is determined by the relative strength of the two microscopic couplings in the arrays. The observed preference of intertoroidal domain walls (green lines) indicates that the intratoroidal coupling dominates over the intertoroidal coupling for both types of arrays.

While in the arrays of composite magnetotoroidal moments both couplings stem purely from the magnetic-dipole interaction and are of comparable magnitude, the interactions in the arrays of monolithic magnetotoroidal moments result from different mechanisms with intrinsically different magnitudes, as described in Sec. V B. As introduced above, the structure of the unit cells in the arrays of composite magnetotoroidal moments allows for two distinct types of domain walls that run either in between or across the composite unit cells as demonstrated in Ref. [26]. Note that, in contrast, the domain walls in arrays of monolithic magnetotoroidal moments can only run in between magnetotoroidal moments that exhibit an opposite magnetic vorticity. Nevertheless, previous work [45,46] indicates that, as a result of the local magnetostatic-energy contribution from the stray fields around a vortex element in densely packed arrays, even the monolithic magnetic vortex state may destabilize in favor of a uniformly magnetized configuration [47]. Hypothetically, intratoroidal walls in arrays of monolithic magnetotoroidal elements may, hence, emerge as a uniform magnetization in the triangles forming the domain

wall. Within the structural parameters chosen for our arrays, however, we did not observe such states.

If both domain-wall types are present in a sample, lower-dimensional domains within the domain walls become possible [26,48]. We found that the three arrays with composite magnetotoroidal moments display such a substructure within the domain walls, as highlighted in Fig. 7, whereas no such substructure was found in the three arrays with monolithic magnetotoroidal moments as we solely observed intertoroidal walls.

Furthermore, it has been shown for the composite-type magnetotoroidal square array that the type of domain wall determines the net magnetization direction of the magnetic moments forming the wall [26]. As a consequence, the meeting points of the two domain-wall types constitute local sinks and sources of magnetic flux, which is associated with emergent magnetic charges of either sign that we found in all our arrays of composite magnetotoroidal moments.

## VI. CONCLUSION

We investigated the spontaneous uniform alignment of magnetic whirls, so-called magnetotoroidal moments, as a type of ferroic order. Our experimental systems are arrays of nanoscale building blocks, made from a soft-magnetic alloy, that we fabricated by electron-beam lithography combined with electron-beam evaporation. With the substitution of the crystal structure and its interactions at the atomic scale with a system of mesoscopic magnets, we achieved an unparalleled local experimental access to the magnetotoroidal state. We distinguish between arrays of composite and monolithic magnetotoroidal moments. While the composite arrays exhibit magnetotoroidal moments that consist of a ringlike arrangement of magnetic single-domain nanobars representing the classical analog to spins, the monolithic arrays consist of ferromagnetic triangles that host an intrinsic magnetotoroidal moment. Using macrospin calculations and micromagnetic simulations, we have quantified the inter- and intratoroidal couplings that promote the emergence of magnetotoroidal order in both types of nanomagnetic arrays.

Using MFM we confirmed the emergence of spontaneous long-range order in our arrays with magnetotoroidal domains that span over a few to several tens of unit cells. Our measurements reveal the presence of two types of domain walls in the arrays of composite magnetotoroidal moments. The walls either run in between or across the toroidal building blocks, which is associated with a dominance of the intra- or intertoroidal coupling, respectively. In the arrays with composite magnetotoroidal moments both the intra- and intertoroidal coupling are determined by the magnetic-dipole interaction. Therefore, both couplings are of similar magnitude and both types of domain walls are observed. In contrast, in the arrays with monolithic magnetotoroidal moments, the intratoroidal coupling, which is given by the interplay of the magnetic-dipole and the magnetic-exchange interaction, inherently dominates so that only intertoroidal walls are observed.

In a more general framework, we shed light on ferroitoroidicity as a new and elusive type of net-magnetization-free long-range magnetic order that spontaneously breaks space-

inversion and time-reversal symmetries. As a consequence, the ferrotoroidic state exhibits the potential for exploitation of its intrinsic linear magnetoelectric effect and unique nonreciprocal optical responses associated with it. Both phenomena are of fundamental interest and could be useful in the development of new functional materials with possible future applicability in memory arrays, sensors, and photonic devices. With the demonstration of spatially resolved magnetotoroidal order in mesoscale magnetic arrays, our work displays the fundamental benefits of utilizing such classical systems for emulating subtle and complex ordering phenomena occurring at the atomic scale.

## ACKNOWLEDGMENTS

The authors thank Th. Lottermoser, A. Bortis, P. M. Derlet, and C. Donnelly for valuable discussions. M.F. acknowledges funding by the Swiss National Science Foundation (Projects No. 200021-175926 and No. 200021-178825) and the European Research Council (advanced Grant No. 694955 INSEETO). J.L. and M.F. acknowledge funding by the ETH Research Grant No. ETH-28 14-1. N.L. and L.J.H. acknowledge funding by the Swiss National Science Foundation (Project No. 200021-155917). N.L. acknowledges funding by the European Union's Horizon 2020 research and innovation program (Marie Skłodowska-Curie Grant No. 844304 LICONAMCO).

## APPENDIX

### 1. Legitimacy of the pairwise-interacting point-dipole approximation for modeling arrays of composite magnetotoroidal moments

#### a. Magnetic coupling in the far field

With Fig. 9 we support and quantify our assumption that nearest-neighbor interactions between the nanomagnetic building blocks in magnetotoroidal arrays are sufficient to explain the domain configuration close to equilibrium. We calculate the interaction energy using Eq. (1) and consider different pairs of pointlike magnetic moments that meet at the vertex of our lattices, as schematically shown in Figs. 4 and 9(a)–9(c). This allows us to evaluate the contribution of far-field couplings to the net interaction energy as shown in Figs. 9(d)–9(f). The model is parameterized by assuming

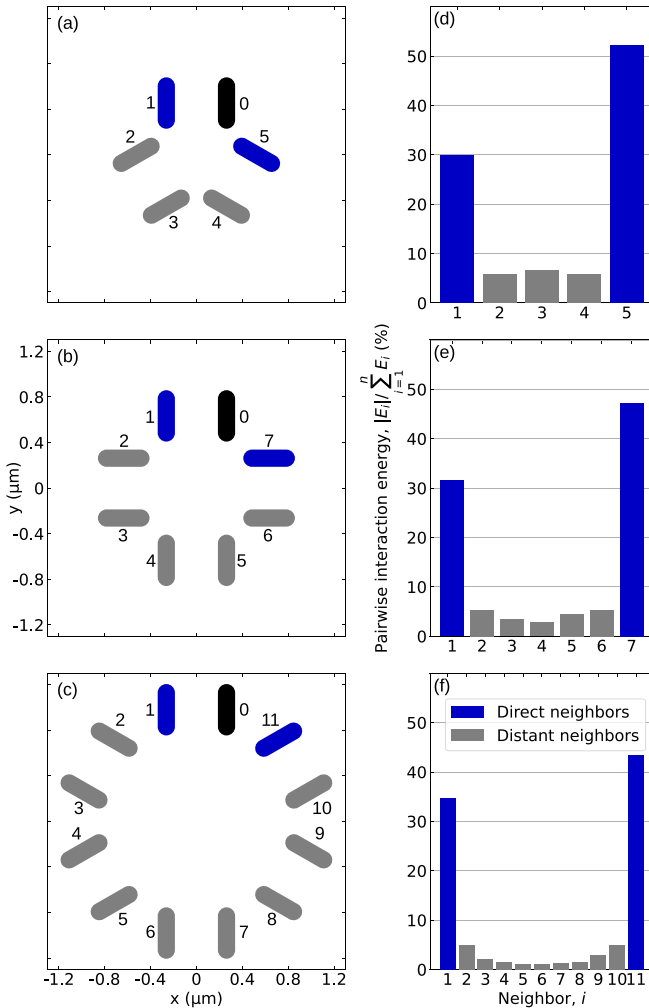


FIG. 9. Pairwise interaction energy between magnets at the vertices of our lattices. [(a)–(c)] Geometric arrangement of magnetic moments on the kagome (a), square (b), and hexagonal (c) lattice; see also Fig. 4. Magnets colored in black indicate the reference magnetic moment for separately calculating the energy associated with the magnetic-dipole interaction with each numbered neighbor. Blue magnets indicate the two nearest neighbors, and gray magnets indicate the neighbors that are further away. [(d)–(f)] Magnetic-dipole-energy contribution for the pairs of point dipoles associated with panels (a), (b) and (c), respectively, with a center-to-center distance between adjacent magnets of 525 nm.

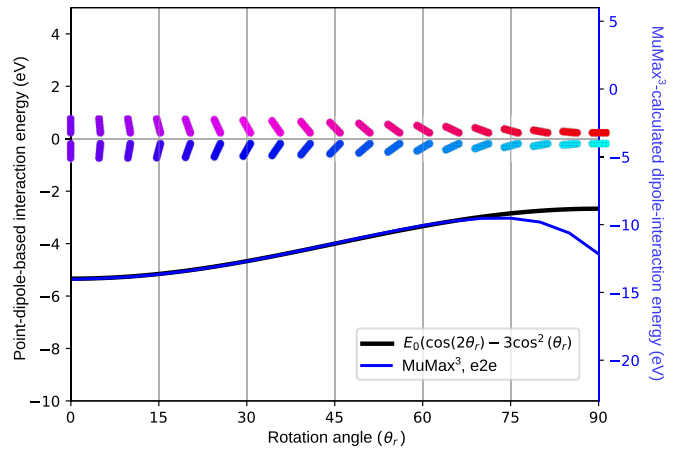


FIG. 10. Interaction energies between pairs of magnets based on different nanomagnetic models. Pairwise interaction energies for the nanomagnet configurations shown in Fig. 4(a). We present our simple point-dipole calculation with a constant center-to-center distance between adjacent nanomagnets of 525 nm (black curve) and the simulated dipole-interaction energies from MuMax<sup>3</sup> [30], assuming a constant edge-to-edge (e2e) distance between adjacent nanomagnets of 75 nm (blue curve). On comparing the two results qualitatively, we see that the simple point-dipole model captures the angle-dependent coupling between pairs of nanomagnets reasonably well.

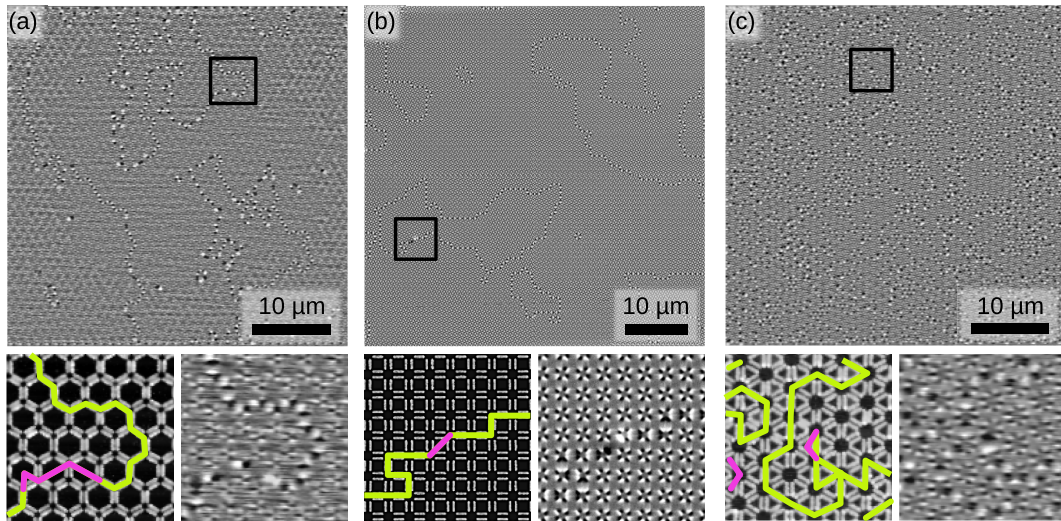


FIG. 11. Long-range order in arrays of composite magnetotoroidal moments. Uncolored raw images of Fig. 7.

stadium-shaped nanomagnets of 450 nm length and 150 nm width, and with 525 nm center-to-center distances between adjacent nanomagnets. For the three arrays with kagome, square, and hexagonal symmetries, the energy contribution from the more-distant neighbors is well below 10% of the total interaction energy per vertex.

### *b. Comparison of point dipoles and spatially extended nanomagnets*

In our derivation of the interaction energies, we approximated the spatially extended magnetic building blocks as point dipoles. To justify this simplification, we calculated the interaction energy for pairs of zero-dimensional point dipoles

and for pairs of three-dimensional stadium-shaped nanomagnets with a finite volume for the nanomagnet configurations as shown in Fig. 4(a). In particular, we performed simulations of nanomagnet configurations with a constant 75 nm edge-to-edge separation rather than a constant 525 nm center-to-center separation between pairs of nanomagnets, reflecting our experimental implementation. The resulting interaction energies as a function of the angle between the nanomagnets are shown in Fig. 10.

### 2. Uncolored MFM scans of magnetotoroidal arrays

The raw MFM scans (without the image processing as described in Sec. IV C) of Figs. 7 and 8 are shown in Figs. 11 and 12, respectively.

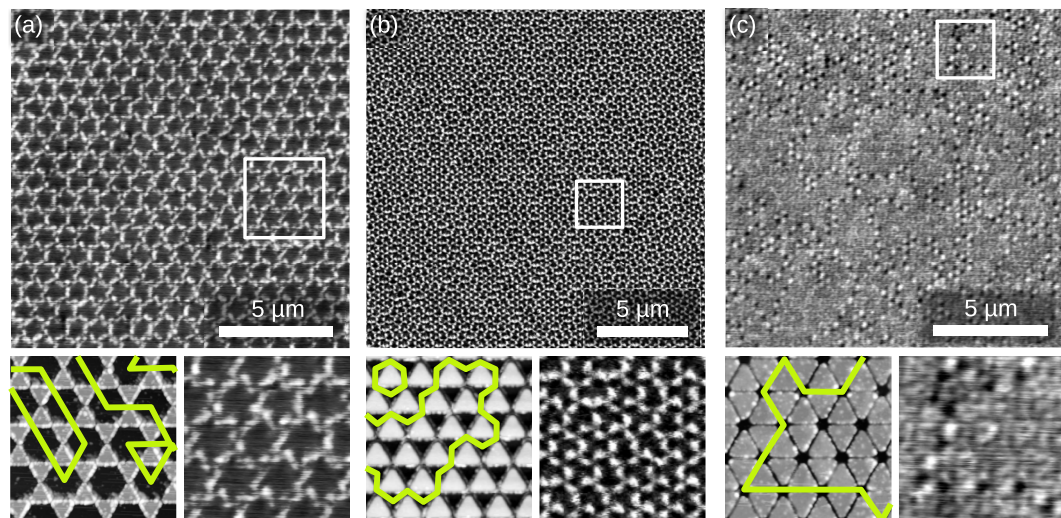


FIG. 12. Long-range order in arrays of monolithic magnetotoroidal moments. Uncolored raw images of Fig. 8.

- [1] K. Aizu, Possible species of ferromagnetic, ferroelectric, and ferroelastic crystals, *Phys. Rev. B* **2**, 754 (1970).
- [2] V. K. Wadhawan, *Introduction to Ferroic Materials*, 1st ed. (CRC Press, Boca Raton, FL, 2000).
- [3] A. K. Tagantsev, L. E. Cross, and J. Fousek, *Domains in Ferroic Crystals and Thin Films* (Springer, New York, 2010).
- [4] N. A. Spaldin, M. Fechner, E. Bousquet, A. Balatsky, and L. Nordström, Monopole-based formalism for the diagonal magnetoelectric response, *Phys. Rev. B* **88**, 094429 (2013).
- [5] W. Jin, E. Druke, S. Li, A. Admasu, R. Owen, M. Day, K. Sun, S.-W. Cheong, and L. Zhao, Observation of a ferro-rotational order coupled with second-order nonlinear optical fields, *Nat. Phys.* **16**, 42 (2020).
- [6] V. Dubovik and V. Tugushev, Toroid moments in electrodynamics and solid-state physics, *Phys. Rep.* **187**, 145 (1990).
- [7] A. A. Gorbatsevich and Y. V. Kopayev, Toroidal order in crystals, *Ferroelectrics* **161**, 321 (1994).
- [8] C. Ederer and N. A. Spaldin, Towards a microscopic theory of toroidal moments in bulk periodic crystals, *Phys. Rev. B* **76**, 214404 (2007).
- [9] N. A. Spaldin, M. Fiebig, and M. Mostovoy, The toroidal moment in condensed-matter physics and its relation to the magnetoelectric effect, *J. Phys.: Condens. Matter* **20**, 434203 (2008).
- [10] Y. V. Kopayev, Toroidal ordering in crystals, *Phys. Usp.* **52**, 1111 (2009).
- [11] S. Gnewuch and E. E. Rodriguez, The fourth ferroic order: Current status on ferrotoroidic materials, *J. Solid State Chem.* **271**, 175 (2019).
- [12] U. Staub, Y. Bodenthin, C. Piamonteze, M. García-Fernández, V. Scagnoli, M. Garganourakis, S. Koohpayeh, D. Fort, and S. W. Lovesey, Parity- and time-odd atomic multipoles in magnetoelectric  $\text{GaFeO}_3$  as seen via soft x-ray Bragg diffraction, *Phys. Rev. B* **80**, 140410(R) (2009).
- [13] V. Scagnoli, U. Staub, Y. Bodenthin, R. A. de Souza, M. García-Fernández, M. Garganourakis, A. T. Boothroyd, D. Prabhakaran, and S. W. Lovesey, Observation of orbital currents in  $\text{CuO}$ , *Science* **332**, 696 (2011).
- [14] M. Fiebig, Revival of the magnetoelectric effect, *J. Phys. D* **38**, R123 (2005).
- [15] F. Thöle, A. Keliri, and N. A. Spaldin, Concepts from the linear magnetoelectric effect that might be useful for antiferromagnetic spintronics, *J. Appl. Phys.* **127**, 213905 (2020).
- [16] H. Watanabe and Y. Yanase, Symmetry analysis of current-induced switching of antiferromagnets, *Phys. Rev. B* **98**, 220412(R) (2018).
- [17] G. L. J. A. Rikken, C. Strohm, and P. Wyder, Observation of Magnetoelectric Directional Anisotropy, *Phys. Rev. Lett.* **89**, 133005 (2002).
- [18] T. Arima, Magnetoelectric optics in non-centrosymmetric ferromagnets, *J. Phys.: Condens. Matter* **20**, 434211 (2008).
- [19] D. Szaller, S. Bordács, and I. Kézsmárki, Symmetry conditions for nonreciprocal light propagation in magnetic crystals, *Phys. Rev. B* **87**, 014421 (2013).
- [20] I. Kézsmárki, D. Szaller, S. Bordács, V. Kocsis, Y. Tokunaga, Y. Taguchi, H. Murakawa, Y. Tokura, H. Engelkamp, T. Rößler, and U. Nagel, One-way transparency of four-coloured spin-wave excitations in multiferroic materials, *Nat. Commun.* **5**, 3203 (2014).
- [21] S. Toyoda, N. Abe, S. Kimura, Y. H. Matsuda, T. Nomura, A. Ikeda, S. Takeyama, and T. Arima, One-Way Transparency of Light in Multiferroic  $\text{CuB}_2\text{O}_4$ , *Phys. Rev. Lett.* **115**, 267207 (2015).
- [22] B. B. Van Aken, J.-P. Rivera, H. Schmid, and M. Fiebig, Observation of ferrotoroidic domains, *Nature (London)* **449**, 702 (2007).
- [23] A. S. Zimmermann, D. Meier, and M. Fiebig, Ferroic nature of magnetic toroidal order, *Nat. Commun.* **5**, 4796 (2014).
- [24] C. Lee, J. Kang, J. Hong, J. H. Shim, and M.-H. Whangbo, Analysis of the difference between the pyroxenes  $\text{LiFeSi}_2\text{O}_6$  and  $\text{LiFeGe}_2\text{O}_6$  in their spin order, spin orientation, and ferrotoroidal order, *Chem. Mater.* **26**, 1745 (2014).
- [25] J. Lehmann, C. Donnelly, P. M. Derlet, L. J. Heyderman, and M. Fiebig, Poling of an artificial magneto-toroidal crystal, *Nat. Nanotechnol.* **14**, 141 (2019).
- [26] J. Lehmann, A. Bortis, P. M. Derlet, C. Donnelly, N. Leo, L. J. Heyderman, and M. Fiebig, Relation between microscopic interactions and macroscopic properties in ferroics, *Nat. Nanotechnol.* **15**, 896 (2020).
- [27] A. B. Harris, A system exhibiting toroidal order, *Phys. Rev. B* **82**, 184401 (2010).
- [28] O. G. Udalov, M. V. Sapozhnikov, E. A. Karashtin, B. A. Gribkov, S. A. Gusev, E. V. Skorohodov, V. V. Rogov, A. Y. Klimov, and A. A. Fraerman, Nonreciprocal light diffraction by a lattice of magnetic vortices, *Phys. Rev. B* **86**, 094416 (2012).
- [29] V. L. Krutyanskiy, I. A. Kolmychek, B. A. Gribkov, E. A. Karashtin, E. V. Skorohodov, and T. V. Murzina, Second harmonic generation in magnetic nanoparticles with vortex magnetic state, *Phys. Rev. B* **88**, 094424 (2013).
- [30] A. Vansteenkiste, J. Leliaert, M. Dvornik, M. Helsen, F. Garcia-Sanchez, and B. Van Waeyenberge, The design and verification of MuMax3, *AIP Adv.* **4**, 107133 (2014).
- [31] X. Zhang, Y. Lao, J. Sklenar, N. S. Bingham, J. T. Batley, J. D. Watts, C. Nisoli, C. Leighton, and P. Schiffer, Understanding thermal annealing of artificial spin ice, *APL Mater.* **7**, 111112 (2019).
- [32] J. M. Luttinger and L. Tisza, Theory of dipole interaction in crystals, *Phys. Rev.* **70**, 954 (1946).
- [33] C. Kraemer, N. Nikseresht, J. O. Piatek, N. Tsyrlin, B. D. Piazza, K. Kiefer, B. Klemke, T. F. Rosenbaum, G. Aeppli, C. Gannarelli, K. Prokes, A. Podlesnyak, T. Strassle, L. Keller, O. Zaharko, K. W. Kramer, and H. M. Ronnow, Dipolar antiferromagnetism and quantum criticality in  $\text{LiErF}_4$ , *Science* **336**, 1416 (2012).
- [34] B. Alkadour, J. I. Mercer, J. P. Whitehead, B. W. Southern, and J. van Lierop, Dipolar ferromagnetism in three-dimensional superlattices of nanoparticles, *Phys. Rev. B* **95**, 214407 (2017).
- [35] R. P. Cowburn, Property variation with shape in magnetic nanoelements, *J. Phys. D* **33**, R1 (2000).
- [36] S. Bedanta and W. Kleemann, Supermagnetism, *J. Phys. D* **42**, 013001 (2009).
- [37] S. H. Skjærvø, C. H. Marrows, R. L. Stamps, and L. J. Heyderman, Advances in artificial spin ice, *Nat. Rev. Phys.* **2**, 13 (2020).
- [38] A. Vogel, A. Corinna Niemann, C. Stenner, A. Drews, M.-Y. Im, P. Fischer, and G. Meier, Vortex dynamics in triangular-shaped confining potentials, *J. Appl. Phys.* **112**, 063916 (2012).

- [39] S. Yakata, M. Miyata, S. Nonoguchi, H. Wada, and T. Kimura, Control of vortex chirality in regular polygonal nanomagnets using in-plane magnetic field, *Appl. Phys. Lett.* **97**, 222503 (2010).
- [40] L. Thevenard, H. Zeng, D. Petit, and R. Cowburn, Macrospin limit and configurational anisotropy in nanoscale permalloy triangles, *J. Magn. Magn. Mater.* **322**, 2152 (2010).
- [41] O. Kazakova, R. Puttock, C. Barton, H. Corte-León, M. Jaafar, V. Neu, and A. Asenjo, Frontiers of magnetic force microscopy, *J. Appl. Phys.* **125**, 060901 (2019).
- [42] M. Jaafar, R. Yanes, D. Perez de Lara, O. Chubykalo-Fesenko, A. Asenjo, E. M. Gonzalez, J. V. Anguita, M. Vazquez, and J. L. Vicent, Control of the chirality and polarity of magnetic vortices in triangular nanodots, *Phys. Rev. B* **81**, 054439 (2010).
- [43] J. P. Morgan, A. Stein, S. Langridge, and C. H. Marrows, Thermal ground-state ordering and elementary excitations in artificial magnetic square ice, *Nat. Phys.* **7**, 75 (2011).
- [44] U. B. Arnalds, J. Chico, H. Stopfel, V. Kapaklis, O. Bärenbold, M. A. Verschuuren, U. Wolff, V. Neu, A. Bergman, and B. Hjörvarsson, A new look on the two-dimensional ising model: Thermal artificial spins, *New J. Phys.* **18**, 023008 (2016).
- [45] A. O. Adeyeye, S. Goolaup, N. Singh, C. C. Wang, X. S. Gao, C. A. Ross, W. Jung, and F. J. Castaño, Magnetostatic coupling in arrays of elongated Ni<sub>80</sub>Fe<sub>20</sub> rings, *J. Phys. D* **40**, 6479 (2007).
- [46] B. E. Skovdal, N. Strandqvist, H. Stopfel, M. Pohlit, T. Warnatz, S. D. Sløetjes, V. Kapaklis, and B. Hjörvarsson, Temperature-induced collapse of spin dimensionality in magnetic metamaterials, *Phys. Rev. B* **104**, 014434 (2021).
- [47] R. P. Cowburn, D. K. Koltsov, A. O. Adeyeye, M. E. Welland, and D. M. Tricker, Single-Domain Circular Nanomagnets, *Phys. Rev. Lett.* **83**, 1042 (1999).
- [48] A. Hubert and R. Schäfer, *Magnetic Domains: The Analysis of Magnetic Microstructures* (Springer, Berlin, 2009).